# Theoretical and Experimental Analysis of a Tuneable Vibration Absorber using Acceleration and Displacement Feedback

**N. Alujević[1], I. Tomac[2], P. Gardonio[3]**
[1] Fraunhofer LBF, KC-MA,
Bartningstrasse 47, 64289 Darmstadt, Germany
FESB, University of Split,
R. Boskovica b.b, 21000 Split, Croatia
email: **neven.alujevic@fesb.hr**

[2] FESB, University of Split,
R. Boskovica b.b, 21000 Split, Croatia

[3] DIEGM Università degli Studi di Udine,
Via delle Scienze, 208 - 33100 Udine, Italy

## Abstract
This study is concerned with the analysis and design of a tuneable vibration absorber, which is composed by a flexible beam with a clamping block in the middle and two masses symmetrically mounted at two ends. The free length of the beam is used to accommodate piezoelectric strain actuators. The two masses at the ends are equipped with inertial accelerometers. Firstly, this arrangement is used to generate two independent acceleration feedback control loops that produce virtual mass effects, which consequently shift the absorbing frequency of the device. Secondly, the accelerometer output is time-integrated twice in order to implement displacement feedback loops that generate virtual changes in the beam stiffness to shift the characteristic frequency of the device. The two feedback approaches are first analysed theoretically, using a mobility-impedance approach, and then experimentally on a prototype absorber unit. The stability of the feedback loops is studied using the Nyquist criterion in order to estimate the limits on the tuneable range of frequencies which are set by the maximum stable feedback gain. The study indicates that the stability margins for the acceleration feedback loops substantially depend on the application of an appropriate low-pass filter. This is due to unfavourably large amplitudes of the sensor-actuator frequency response functions at higher frequencies. In contrast, implementation of displacement feedback naturally yields a favourable roll-off at higher frequencies and gives better stability margins. The maximum feedback gain is however limited at low-frequencies due to the frequency response of the analogue double-integrator. Nevertheless, the use of an integrator with a cut-off frequency low enough results in good stability margins that allow for a relatively large shift of the characteristic frequency of the absorber by the active displacement feedback control.

## 1 Introduction

Vibration absorbers are essentially base-excited one degree of freedom mass-spring resonator systems with appropriately adjusted mass-stiffness ratio. The driving point accelerance at the base has a zero which is the absorber characteristic frequency. This fact can be used to attenuate vibrations of a structure linked to the absorber through the resonator spring [1,2]. The absorber efficiency is limited to the frequency band close to the zero of the driving point accelerance function. The width of this frequency band depends on the damping ratio of the absorber. Generally, the lower is the damping; the narrower is the frequency range where the attenuation occurs [1-4].

Vibration absorbers can be used for solving vibration-related problems belonging to two broad groups. The first group includes vibrations of flexible structures with a marked resonance peak that requires attenuation. The second group includes rigid structures excited at a single forcing frequency. Traditionally the problems of the first group have drawn more interest [3]. In this case it is important to optimally adjust the damping ratio of the absorber with respect to the mass ratio between the absorber and the vibrating structure, in order to avoid excessive vibration amplification in the vicinity of the troublesome structural resonance [4]. This reduces the peak performance of the attenuation while generating optimal broadband reductions [4]. In contrast, problems belonging to the second group require quite a different set of the optimum parameters, as the vibrations are excited only at the forcing frequency [5,6]. With respect to this, efforts have been made recently to make the device resonant frequency tuneable in order to track the excitation frequency [6-19]. The tuning can be achieved mechanically: for example by changing the arm of cantilevered masses with beam type absorbers [11], or by altering the effective number of coils in the spring with mass-spring type absorbers [12,13]. It can also be achieved by using controllable "smart" materials such as shape memory alloys [14,15]. Furthermore, the tuning can be achieved electrically: for example by means of shunted piezo-elements whose electrical boundary conditions can change the effective stiffness of the material [16-19]. Finally, the tuning can be achieved actively, by means of a control force actuator that acts in parallel with the absorber spring. Then an absolute acceleration sensor at the absorber mass, or a relative stroke sensor between the mass and the vibrating structure, can be used to implement an acceleration or displacement feedback loop [20-23] which consequently generates a virtual mass or stiffness change, respectively. Furthermore, attempts have been done to adjust the damping ratio of the absorber by means of a positive velocity feedback to reduce the damping for increasing the peak performance [22].

The use of stroke or acceleration sensors in conjunction with the control force can be viewed as a collocated control. However, such a sensor and actuator pair is not dual so that they do not produce energy absorption, which would guarantee unconditional stability [24]. Therefore, the stability of such acceleration or displacement feedback loops is limited by maximum stable feedback gains, which determine the maximum shift of the absorber input accelerance zero and thus influence the adaptability of the device.

In this paper a beam type tuneable vibration absorber is considered, which is made of a flexible beam with a clamping block in the middle and two masses symmetrically mounted at the two beam ends. Two control designs are considered. For both designs, the free length of the beam is used to accommodate piezoelectric strain actuators and the two masses are equipped with inertial accelerometers. For the first control design the accelerometer outputs are used to generate two independent negative acceleration feedback control loops that produce virtual mass effects, which result in a downward shift of the characteristic frequency of the device. The second design considers acceleration signals passed through a double time-integrator. This arrangement is used to generate positive displacement feedback loops that generate a virtual reduction in beam stiffness and thus reduce the characteristic frequency.

The paper is structured in four sections. Section 2 describes the system and provides the mathematical formulation for the theoretical study. In Section 3 the stability and adaptability study for the acceleration feedback is presented, whereas in Section 4 the stability and adaptability study is given for the displacement feedback approach. There are two appendices, Appendix A and Appendix B which describe respectively mobility and impedance matrices and functions used for the mathematical formulation of the problem.

## 2 System studied and mathematical model

The vibration absorber considered in this study consists of a flexible beam with two cantilevered masses at the beam ends. The beam is clamped in the middle via a mounting block where it is supposed to be attached to the primary vibrating structure. The free length of the beam is used to accommodate piezoelectric actuators, and the masses are equipped with inertial accelerometers (Figure 1). The accelerometer outputs are used to provide error signals for driving two piezoelectric patch actuators in order to create two independent feedback loops. Two feedback configurations are considered: a) direct

acceleration feedback, and b) the feedback of double-integrated accelerometer outputs which is equivalent to displacement feedback (Figure 1).

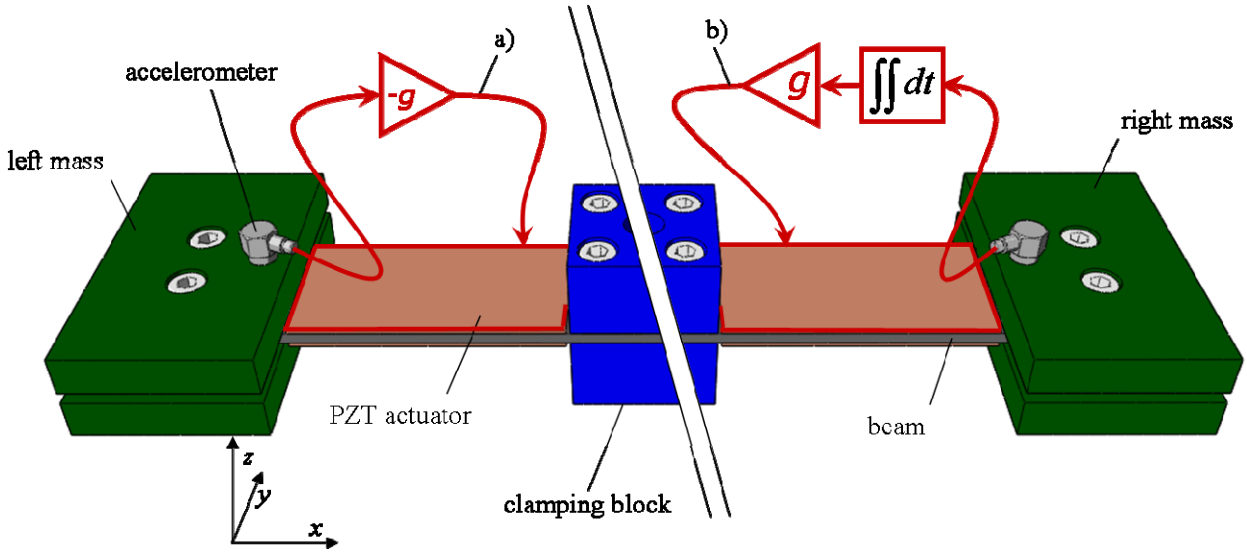


**Figure 1: The two tuneable vibration absorber design schemes: a) direct acceleration feedback, b) direct displacement feedback.**

The theoretical study was performed using a mathematical model based on a mobility-impedance approach [25]. The system was modelled assuming that only the bending vibrations along the beam length are significant. It is assumed that the absorber can be modelled as a finite free-free Euler-Bernoulli beam with added rigid masses at the two ends and in the middle. The excitation of the beam via each piezoelectric actuator is modelled as a moment pair excitation.

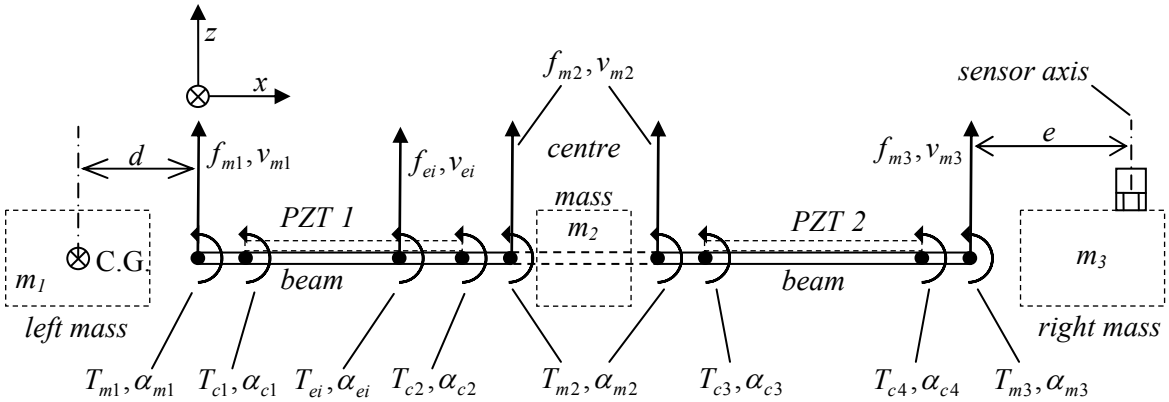


**Figure 2: The mobility model scheme.**

The mass and stiffness added by the two piezoelectric patches is neglected. The effects of the proof masses at the beam ends and in the middle are taken into account by applying appropriate inertial effects at the points of attachment along the beam, as shown in Figure 2. For example, the left mass is modelled as an inertial force and an inertial moment, $f_{m1}$, and $T_{m1}$, acting at the left end of the beam (Figure 2), depending on the linear and angular velocity of the beam at the left end via appropriate impedance functions. In total, there are three relevant locations along the beam with respect to the inertial effects of the lumped masses attached to the beam, and four relevant locations with respect to the active moments exerted onto the beam by the two piezoelectric actuators (Figure 2). In addition to these seven locations, linear and angular velocities at a number of extra points along the beam were also considered to reconstruct the beam deflection shapes. Thus, the beam was divided into a number of $N$ elements, and the

linear and angular velocities at the element centres, $T_{ei}, \alpha_{ei}$ (Figure 2) were included into the formulation. All relevant locations are defined via the following *x* coordinates, grouped together into the location vector **x**:

$$\mathbf{x} = [x_{m1} \quad x_{m2} \quad x_{m3} \quad x_{c1} \quad x_{c2} \quad \cdots \quad x_{c4} \quad x_{e1} \quad x_{e2} \quad \ldots \quad x_{eN}]^T . \tag{1}$$

The linear and angular out of plane velocities at the locations defined by Equation (1) are grouped into the beam velocity vector, $\mathbf{v}$. Also the external bending forces and moments are grouped into the external force vector, $\mathbf{f}$, and the impedance forces and moments due to the attached masses are grouped into the impedance force vector $\mathbf{f'}$:

$$\mathbf{v} = \begin{bmatrix} \mathbf{V} \\ \boldsymbol{\alpha} \end{bmatrix} = [v_{m1} \; v_{m2} \; v_{m3} \; v_{c1} \; v_{c2} \; \ldots \; v_{c4} \; v_{e1} \; v_{e2} \; \ldots \; v_{eN} \; \alpha_{m1} \; \alpha_{m2} \; \alpha_{m3} \; \alpha_{c1} \; \alpha_{c2} \; \ldots \; \alpha_{c4} \; \alpha_{e1} \; \alpha_{e2} \; \ldots \; \alpha_{eN}]^T , \tag{2a}$$

$$\mathbf{f} = \begin{bmatrix} \mathbf{f} \\ \mathbf{t} \end{bmatrix} = [f_{m1} \; f_{m2} \; f_{m3} \; f_{c1} \; f_{c2} \; \ldots \; f_{c4} \; f_{e1} \; f_{e2} \; \ldots \; f_{eN} \; T_{m1} \; T_{m2} \; T_{m3} \; T_{c1} \; T_{c2} \; \ldots \; T_{c4} \; T_{e1} \; T_{e2} \; \ldots \; T_{eN}]^T , \tag{2b}$$

$$\mathbf{f'} = \begin{bmatrix} \mathbf{f'} \\ \mathbf{t'} \end{bmatrix} = [f'_{m1} \; f'_{m2} \; f'_{m3} \; f'_{c1} \; f'_{c2} \; \ldots \; f'_{c4} \; f'_{e1} \; f'_{e2} \; \ldots \; f'_{eN} \; T'_{m1} \; T'_{m2} \; T'_{m3} \; T'_{c1} \; T'_{c2} \; \ldots \; T'_{c4} \; T'_{e1} \; T'_{e2} \; \ldots \; T'_{eN}]^T . \tag{2c}$$

The velocity vector, $\mathbf{v}$, can be expressed as a function of the two force vectors, $\mathbf{f}$ and $\mathbf{f'}$ as follows:

$$\mathbf{v} = \mathbf{Y}\mathbf{f} + \mathbf{Y}\mathbf{f'} , \tag{3}$$

where the matrix $\mathbf{Y}$ is the beam mobility matrix. The matrix $\mathbf{Y}$ can be subdivided into four matrices as follows:

$$\mathbf{Y} = \begin{bmatrix} \mathbf{Y}^{v,f} & \mathbf{Y}^{v,t} \\ \mathbf{Y}^{\alpha,f} & \mathbf{Y}^{\alpha,t} \end{bmatrix} , \tag{4}$$

where $\mathbf{Y}^{v,f}$ is the mobility matrix between the velocities and forces, $\mathbf{Y}^{v,t}$ is the mobility matrix between the velocities and moments, $\mathbf{Y}^{\alpha,f}$ is the mobility matrix between the angular velocities and forces, and finally $\mathbf{Y}^{\alpha,t}$ is the mobility matrix between the angular velocities and bending moments. Expressions for the matrices $\mathbf{Y}^{v,f}$, $\mathbf{Y}^{\alpha,f}$, $\mathbf{Y}^{v,t}$ and $\mathbf{Y}^{\alpha,t}$ are given in Appendix A.

The impedance force vector can be related to the velocity vector via an impedance matrix:

$$\mathbf{F'} = \mathbf{Z}\mathbf{V} . \tag{5}$$

where the impedance matrix $\mathbf{Z}$ is given in Appendix B.

Substitution of Equation (5) into Equation (3) yields:

$$\mathbf{V} = \mathbf{Y}\mathbf{F} + \mathbf{Y}\mathbf{Z}\mathbf{V} , \tag{6}$$

which can be manipulated to give:

$$\mathbf{V} = (\mathbf{I} - \mathbf{Y}\mathbf{Z})^{-1}\mathbf{Y}\mathbf{F} . \tag{7}$$

The term $(\mathbf{I} - \mathbf{Y}\mathbf{Z})^{-1}\mathbf{Y}$ in Equation (7) represents a matrix containing mobility functions of the absorber with the three masses attached to the beam and it is designated as $\mathbf{Q}$, such that Equation (7) can be expressed as:

$$\mathbf{V} = \mathbf{Q}\mathbf{F} \tag{8}$$

The velocities of the absorber at the locations defined by Equation (1) with active forces generated by the two piezoelectric actuators can be expressed as follows:

$$\mathbf{V}_{\mathbf{active}} = \mathbf{Q}\mathbf{F} + \mathbf{Q}\mathbf{F}_{\mathbf{active}} , \tag{9}$$

where

$$\mathbf{F}_{\mathbf{active}} = \mathbf{G}\mathbf{V}_{\mathbf{active}}, \tag{10}$$

and the (14+*N*)×(14+*N*) matrix $\mathbf{G}$ defines the control law, whereas $\mathbf{F}_{\mathbf{active}}$ and $\mathbf{V}_{\mathbf{active}}$ are vectors containing forces/moments and linear/angular velocities at locations defined by Equation (1). These (14+*N*)×1 vectors have the same layout as force and velocity vectors in Equations (2a,b). In case of direct acceleration feedback, the matrix $\mathbf{G}$ has the following non-zero elements:

$$\begin{aligned} &G_{11,1} = -j\omega g, G_{12,1} = j\omega g, G_{13,3} = -j\omega g, G_{14,3} = j\omega g, \\ &G_{11,8} = j\omega ge, G_{12,8} = -j\omega ge, G_{13,10} = -gj\omega e, G_{14,10} = j\omega ge \end{aligned}, \tag{11a-h}$$

where *g* is the feedback gain, and *e* is the absolute value of the distance along *x*-axis between the sensor sensitive axis and the beam end (see Figure 2). For the implementation of displacement feedback, the right hand side terms in each of Equations (11a-h) are multiplied by the double integrator transfer function, $1/(j\omega\tau/2\pi+1)^2$ where the time constant $\tau$ equals to 10 s, yielding the integrator cut-off frequency of 0.1 Hz.

Substitution of Equation (10) into Equation (9) yields:

$$\mathbf{V}_{\mathbf{active}} = \mathbf{QF} + \mathbf{QGV}_{\mathbf{active}}, \tag{12}$$

which can be manipulated to give:

$$\mathbf{V}_{\mathbf{active}} = (\mathbf{I} - \mathbf{QG})^{-1}\mathbf{QF}. \tag{13}$$

The term $(\mathbf{I} - \mathbf{QG})^{-1}\mathbf{Y}$ in Equation (13) represents the matrix containing mobility functions of the absorber with the two feedback loops closed and it is designated as $\mathbf{R} = (\mathbf{I} - \mathbf{QG})^{-1}\mathbf{Q}$, such that Equation (13) can be expressed as:

$$\mathbf{V}_{\mathbf{active}} = \mathbf{TF}. \tag{14}$$

where the matrix $\mathbf{T}$ contains mobility functions of the closed loop absorber, and its element $T_{2,2}$ is effectively the closed-loop absorber input mobility at the attachment point in the middle.

| Parameter | | Value |
|---|---|---|
| Beam free length | $l_x$ | 2×52 mm |
| Beam width | $l_y$ | 30 mm |
| Beam thickness | $t$ | 3 mm |
| Beam mass density | $\rho_b$ | 7800 kg/m$^3$ |
| Beam Young's modulus | $E_r$ | 210·10$^9$ N/m$^2$ |
| Beam Poisson's ratio | $\nu_r$ | 0.3 |
| Beam loss factor | $\eta_r$ | 0.01 |
| Total cantilevered mass | $m$ | 2×0.571 kg |
| Total mass moment of inertia along *y*-axis at the clamping line | $I_{yy}$ | 0.00043 kgm$^2$ |
| Upper/lower mass dimensions | $l_m \times w_m \times h_m$ | 46×75×10 mm$^3$ |
| Mounting interface total mass | $m_i$ | 0.7 kg |
| Upper mounting interface dimensions | $l_{ui} \times w_{ui} \times h_{ui}$ | 35×40×20 mm$^3$ |
| Lower mounting interface dimensions | $l_{ui} \times w_{ui} \times h_{ui}$ | 35×40×20 mm$^3$ |
| Piezoelectric actuator dimensions (PIC 151) | $l_{PZT} \times w_{PZT} \times h_{PZT}$ | 50×30×1 mm$^3$ |
| Mass CG distance from the beam edge | $d$ | 23 mm |
| Accelerometer sensitive axis distance from the beam edge | $e$ | 35 mm |

**Table 1: Geometrical and material properties of the vibration absorber**

Table 1 summarizes the physical properties of the prototype absorber (Figure 6) that have been used for the simulation study. The design with the listed parameters yields the characteristic frequency of about 62 Hz, and the input accelerance at the absorber mounting point has a zero at that frequency (see Figure 5, black lines).

## 3 Negative acceleration feedback

The acceleration feedback approach is first studied with respect to the feedback control stability. This is done by applying the Nyquist criterion on the sensor-actuator open-loop frequency response function (FRF) of one of the two feedback loops. (The theoretical model assumes full symmetry.) Figure 3 shows Bode and Nyquist plots of the frequency response function between the voltage applied to the left piezoelectric actuator and the acceleration at the left block mass. The accelerometer dynamics is neglected. As shown by the blue lines, the phase is contained between 0 and 180 degrees up to approximately 4 kHz. Thus the sensor and actuator behave as a collocated pair. Above this frequency the phase lags further and it is no longer confined between 0 and 180 degrees. This additional lag can be attributed to the non-perfect collocation of the sensor-actuator pair, since the accelerometer measures linear acceleration whereas the piezoelectric actuator generates two bending moments. A closer approximation of the fully collocated sensor would require measuring the difference between two angular velocities at the two ends of the actuator. Such an arrangement is not considered in this study for feasibility reasons. At 6.5 kHz the locus depicted in the Nyquist plot crosses the negative real axis in the point highlighted by the black × symbol in the Bode plot.

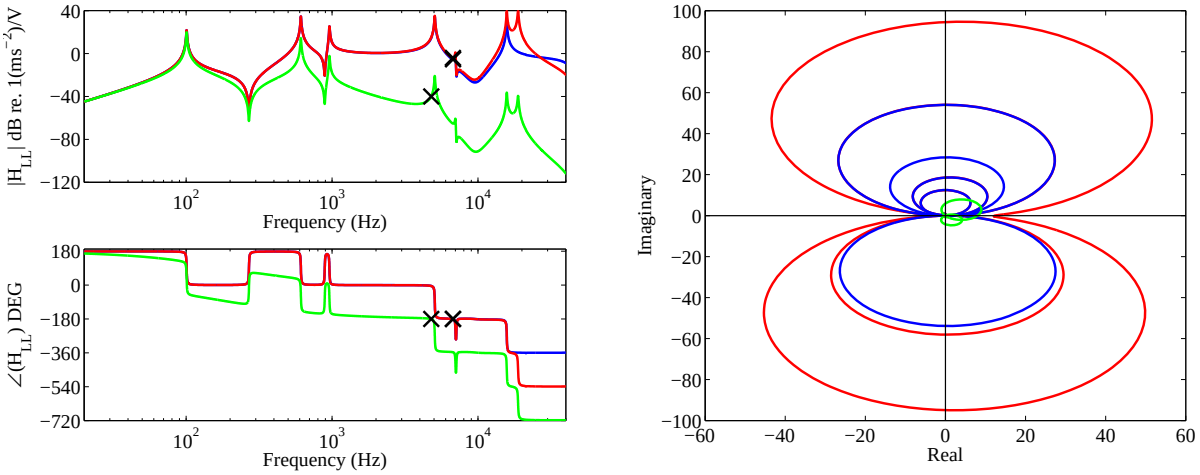


**Figure 3: Bode and Nyquist plots for the sensor-actuator open-loop frequency response functions: considering a) an ideal accelerometer (blue), b) an inertial accelerometer (red), and c) an inertial accelerometer with a second order low-pass filter having a 200 Hz cut-off frequency (green).**

The amplitude of the open-loop FRF at this frequency determines the gain margin in case the other loop is left open. As shown later in the paper, this gain margin is rather low and does not allow for a large shift of the absorber characteristic frequency (see Figure 5, blue lines). The red lines in Figure 3 are for the simulation including the inertial accelerometer dynamic response. The accelerometer has been modelled as a one degree of freedom system and the parameters of the system have been chosen to match a real accelerometer calibration chart. As can be seen in the Bode plots, an additional resonance peak and a -180 degree phase shift occurs due to the accelerometer resonance at about 17 kHz, but no significant stability margin changes can be observed. However considering either the ideal or inertial accelerometer the amplitude of the sensor-actuator open loop FRF increases with frequency. This is a natural property of any accelerance function and it is not a consequence of the sensor-actuator physical match (collocation). Since the two transducers behave as fully collocated only at lower frequencies, and also the control is aimed to shift the rather low characteristic frequency of 62 Hz, this amplitude behaviour is rather unfavourable. For

this reason an attempt is made to filter out the high-frequency output of the sensor. This is not a straightforward task, because any filter introduces also a phase shift. In particular, a low-pass Butterworth filter induces a phase change of -90 degrees per filter order across the cut-off frequency. For this study several filters were tested, and after a careful consideration a second order Butterworth filter was selected with a cut-off frequency of 200 Hz. The implementation of this filter yields the open loop sensor-actuator FRF depicted by the green line in Figure 3. As shown in the Bode plots, the amplitude now rolls-off quickly with frequency such that the largest resonance peak is due to the lowest resonance at around 100 Hz. This is a desirable property for stability as the amplitude at the cross-over point, marked by the black × symbol, is significantly reduced. However, as shown in the phase plot, the phase lags with frequency, and the locus in the Nyquist plot is rotated clockwise towards the right hand side quadrants, entering the damping-like region of the $\Re - \Im$ plane, as shown by the green line in the Nyquist plot in Figure 3.

The stability study on one channel helps to explain the sensor-actuator dynamical coupling, yet, it is not a valid criterion to establish the stability of the whole system, which is composed by two channels that operate simultaneously. This is because of the cross-talk between the two control loops. To asses the stability of the two channel system the generalised Nyquist criterion should be used. In this case the generalised stability study is carried out in terms of the eigenvalues of the return difference matrix $\mathbf{QG}$, where the off-diagonal elements of the matrix $\mathbf{Q}$ contain the cross-talk frequency response functions. The return difference matrix in this case has two eigenvalues and the larger one is relevant for the multichannel system stability. In fact, the classical one channel Nyquist stability criterion can be applied onto the locus of the larger eigenvalue in order to determine the available gain margin of the multichannel system [26]. Figure 4 shows Bode and Nyquist plots of the larger eigenvalue $E_2(\omega)$ for the same three cases studied previously, i.e. the blue lines are for the ideal accelerometer, the red lines are for the inertial accelerometer, and the green lines are for the inertial accelerometer with filtered output. It can be seen that qualitatively the shapes of these Bode and Nyquist plots are similar to Bode and Nyquist plots of the single channel open loop sensor-actuator FRFs, and that the locus crosses over the negative real axis at similar frequencies. The total gain margin is however lowered by about 4 dB. This gain margin can be used to determine the maximum feedback gain in the two loops operating simultaneously.

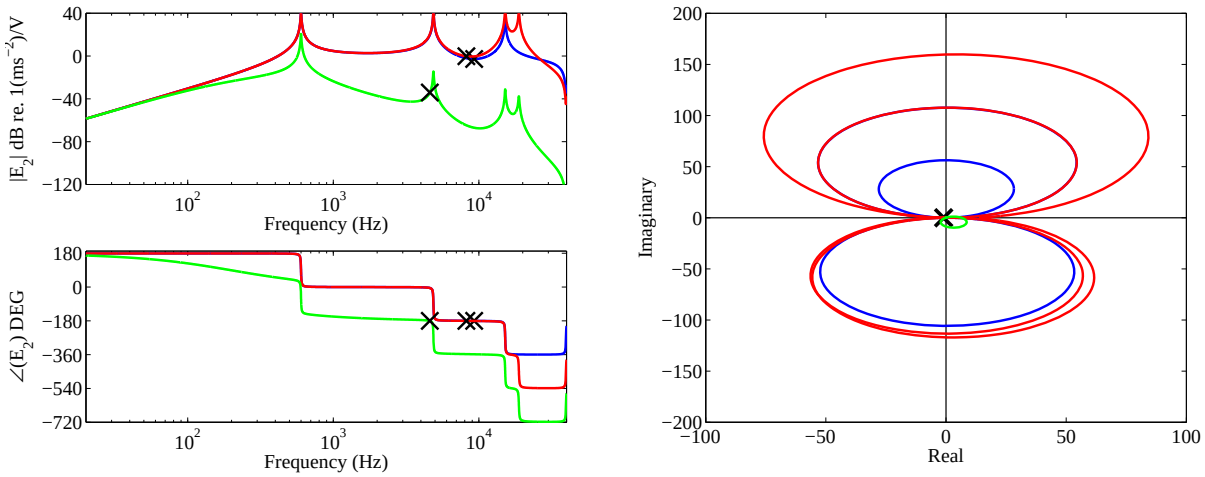


**Figure 4: Bode and Nyquist plots of the larger eigenvalue of the return difference matrix $\mathbf{QG}$: using an ideal accelerometer (blue), inertial accelerometer (red), and inertial accelerometer with a second order low-pass filter having a 200 Hz cut-off frequency (green).**

The simulated input accelerance for the passive system and for the system with control is plotted on the left hand side plot in Figure 5. The passive absorber accelerance is shown using the black line, whereas the active absorber input accelerance, with feedback loops applying the maximum feedback gain that still yields stable loops, is plotted using the same coloured lines as in Figure 3 and Figure 4 with respect to the three cases studied.

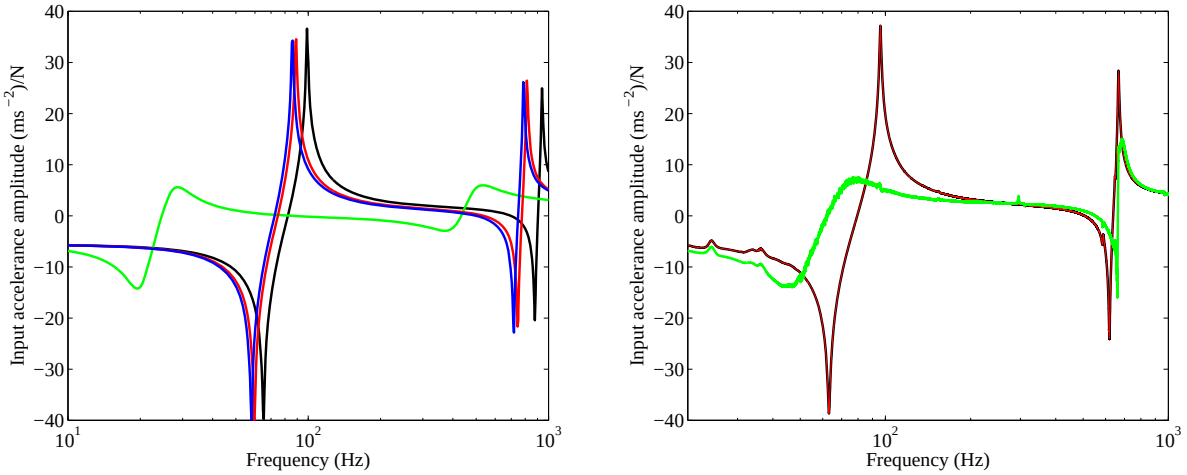


**Figure 5: Input accelerance at the absorber mounting point with open loops (black line), and closed loops using the maximum stable feedback gain. The closed loop accelerance is shown using an ideal accelerometer (blue), inertial accelerometer (red), and inertial accelerometer with a second order low-pass filter having a 200 Hz cut-off frequency (green). The left plot is theoretical and the right plot is experimental.**

As shown by the blue and red lines, the maximum downward shift of the characteristic frequency (the antiresonance at 62 Hz) is of the order of few Hertz. This shifting could probably be used for minor tuning in applications where the primary structure is excited at constant frequencies that can only slightly vary. For example, an air-conditioning unit compressor rotation speed will typically vary by few Hertz due to changes in loading conditions [22,23]. However, a larger variation in the rotation speed could not be followed. In contrast, the filtered acceleration feedback gives a larger shift of almost -40 Hz, as shown by the green line. However it can be seen that the filtering of the accelerometer output (that rotated the locus of the sensor-actuator open loop FRF in Figure 3 towards the damping region of the $\Re - \Im$ plane) actually generates a damping effect.

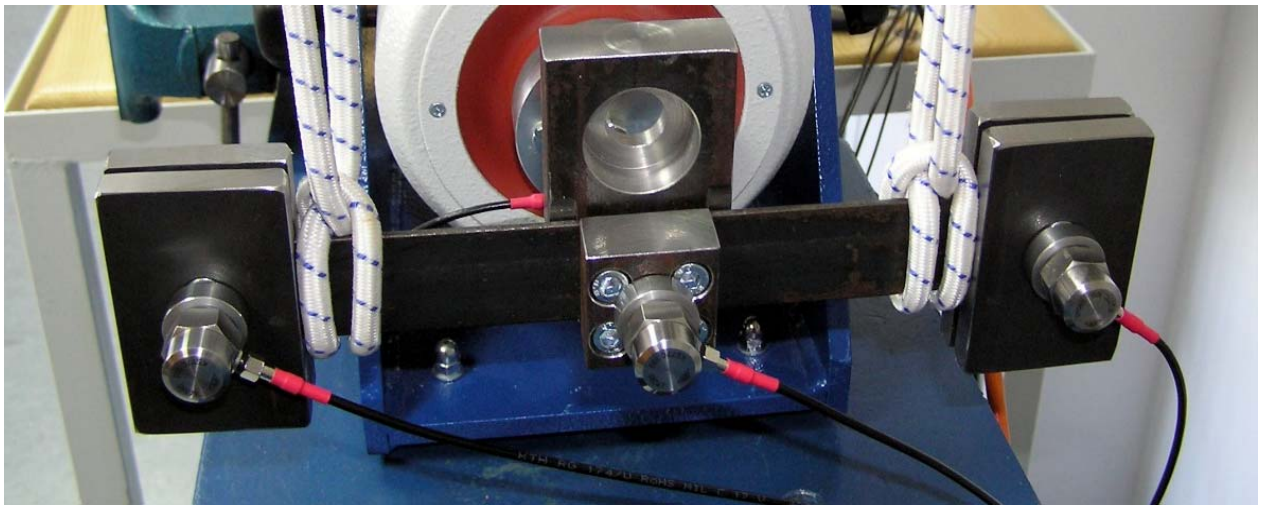

**Figure 6: The prototype absorber.**

In fact, the absorber response is so damped that the amplitude of the input accelerance function goes up by 25 dB. Thus it can be stated that the filtering of the accelerometer output generates a combined effect of a negative acceleration and a negative velocity feedback. This is not a favourable behaviour since the aim of the active control is to shift the characteristic frequency while keeping the favourable low damping that

gives the high input impedance (the low input accelerance) of the absorber. It is probably possible to increase the cut-off frequency of the filter and to reduce the damping effect, but this would also reduce the gain margin and thus the maximum shift of the characteristic frequency of the absorber.

The simulation study is backed up by an experimental analysis performed on the prototype absorber that is shown in Figure 6. The prototype was equipped with an additional accelerometer in the middle and attached to the shaker through a force gauge in order to measure the input accelerance passively and under control. The measured open-loop sensor-actuator FRFs are shown up to 1 kHz in Figure 7.

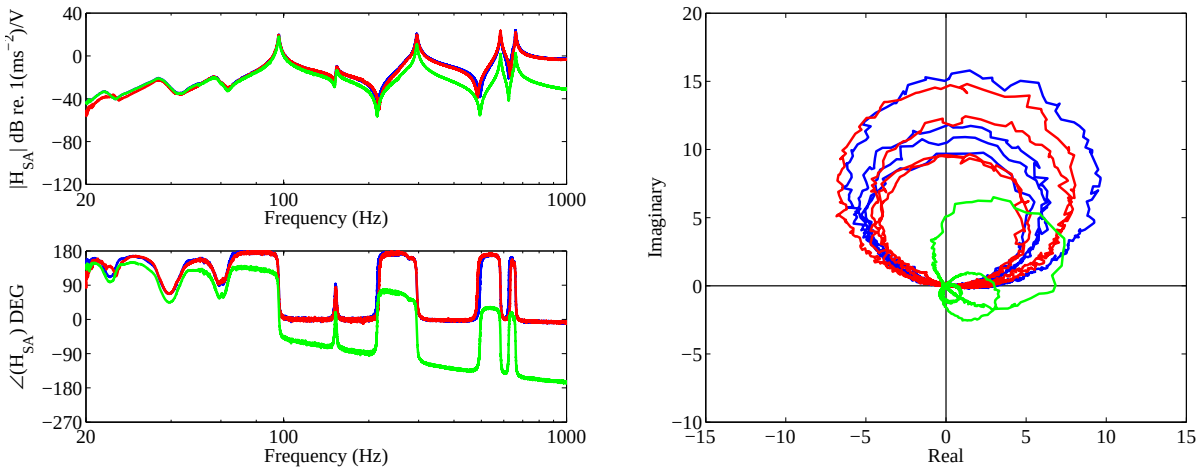


**Figure 7: The Bode and Nyquist plots of the experimentally determined open-loop sensor-actuator FRF up to 1 kHz. Blue lines are for the left feedback loop and red lines are for the right feedback loop. The green lines are for the left feedback loop with filtered output.**

The blue and the red lines are for the left and the right feedback loop, whereas the green line is for the left feedback loop with low-pass filtering. As shown by the blue and red lines the left and right feedback loops are practically the same due to the symmetrical design of the tuneable absorber. Furthermore, the phase is contained between 180 and 0 degrees, which suggests that also in practice the sensor and actuator behave as collocated pairs at low frequencies. The implementation of the low-pass filter yielded the amplitude roll-off and the phase lag as anticipated by the simulation study (green lines). The aim of showing the result up to 1 kHz is to illustrate that the feedback loop delivers the virtual mass at low frequencies where the control is actually aimed at. However, as shown in Figure 8, this property is lost at higher frequencies above approximately 1 kHz as the phase of the sensor-actuator open loop FRF lags considerably, especially at frequencies above 3 kHz. In accordance to what can be observed using the simulation study results, the amplitudes at higher frequencies are increasing, reaching the peak around the accelerometer resonance (17 kHz), and then gradually reducing as the accelerometer output above its fundamental resonance abruptly decreases. Therefore to have good stability properties the low-pass filtering is necessary to reduce the large frequency amplitudes. Thus the low-pass filter that was considered in the simulation studies has been applied and the result is shown by the green lines in Figure 8. The Nyquist plot in Figure 8 shows that without filtering (blue and red lines) the available gain margin is relatively low as the locus crosses the negative real axis with large amplitudes of approximately 400 ms$^{-2}$/V. With filtering, the high frequency amplitudes decrease, but at cost of an additional phase lag due to the filter transfer function (green lines). In order to determine the maximum stable feedback gain, the generalised Nyquist criterion was applied by analysing the eigenvalues of the return difference matrix obtained experimentally for the case of low-pass filtered accelerometer outputs. The Bode and Nyquist plots of both eigenvalues are shown in Figure 9. As can be seen in the Nyquist plot, the negative real axis cross-over now occurs at much lower amplitude, such that larger feedback gains can be implemented without compromising the stability. Yet, the loci of both eigenvalues are rotated clockwise and thus the combined effects of the two feedback loops deliver a mixture of active mass and active damping. This is clearly visible in the right hand side plot of Figure 5 where the green lines show a shift of the characteristic

frequency of about 20 Hz, but the amplitude of the accelerance is significantly increased due to the added active damping.

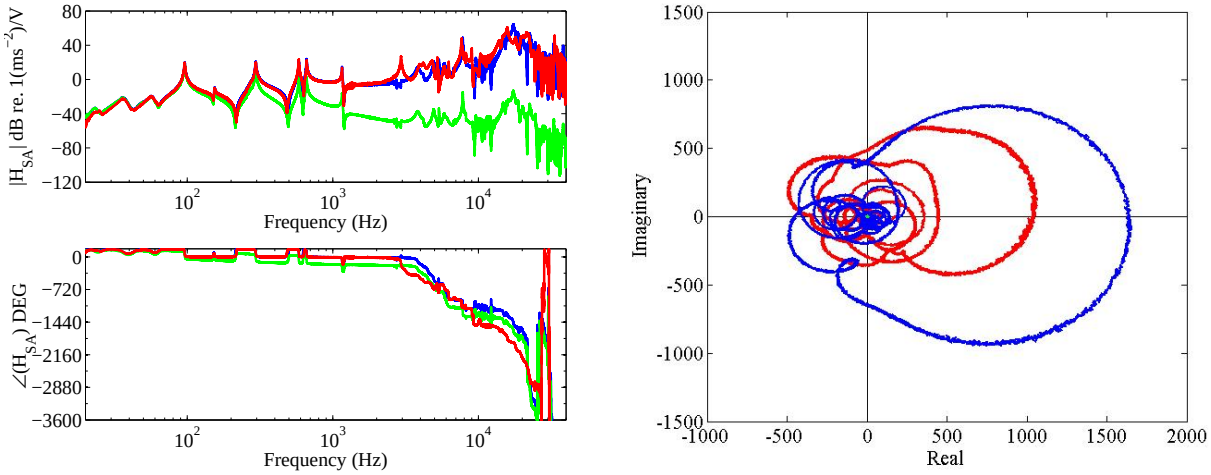


**Figure 8: The Bode and Nyquist plots of the experimentally determined open-loop sensor-actuator FRF up to 40 kHz. Blue lines are for the left feedback loop and red lines are for the right feedback loop. The green lines are for the left feedback loop with filtered output.**

As previously mentioned this is an adverse effect as a lightly damped input accelerance zero is necessary for good vibration absorption. In conclusion, it can be stated that the acceleration feedback, although theoretically possible, in practice fails due to the intrinsic property of the open loop sensor-actuator frequency response functions which exhibit amplitudes increasing with frequency. This causes stability problems as the sensor-actuator pair do not behave as collocated at high frequency. Furthermore, the control is aimed at shifting the rather low-frequency zero of the absorber input accelerance while the open loop sensor-actuator FRF shows only small amplitudes at low frequencies.

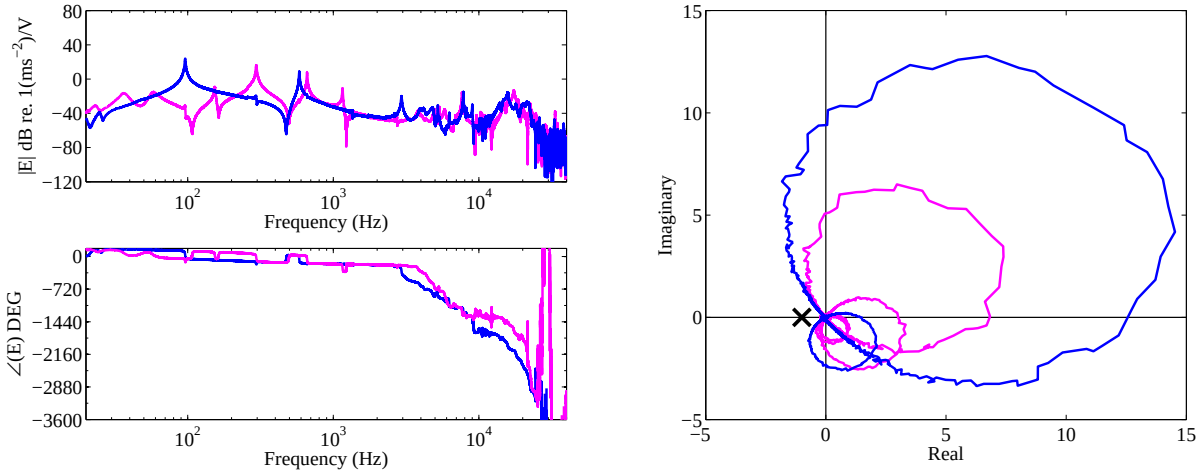


**Figure 9: Bode and Nyquist plots of the two eigenvalues of the return difference matrix QG obtained experimentally with applied a second order low-pass filter having a 200 Hz cut-off frequency.**

For example the black and the red lines in the right hand side plot of Figure 5 perfectly overlap, meaning that the available feedback gain yields no shift of the characteristic frequency. The filtering attempt results in a considerable improvement in the available feedback gain, however at cost of delivering the undesirable damping effect.

For all theses reasons an alternative feedback configuration is studied in the following Section 4. The error signal chosen is a double integrated acceleration with respect to time which is equivalent to displacement. Such a feedback control should yield a shift of the characteristic frequency by generating an active stiffness effect. Furthermore, it is known that receptances roll-off steeply with frequency [25], which should result in adequate stability margins without heavy filtering, since the higher frequency imperfections of the sensor-actuator pair collocation should be less influential due to the reduced amplitudes.

## 4 Positive displacement feedback

In order to downwardly shift of the absorber resonant frequencies the beam stiffness should be artificially decreased. This could be achieved with positive displacement feedback loops. The absolute displacement at the end of the beam can be approximated by double integrated acceleration with respect to time. Therefore the same experimental setup can be used with the addition of a double integrator analogue filter. For the experimental study the double integrator available with the charge amplifiers for conditioning accelerometer signals was used, which has a cut-off frequency of 0.1 Hz. Also in this case, a simulation study is performed first aiming to investigate the stability of a single feedback loop using the Nyquist criterion. The open loop sensor-actuator FRF is depicted in Figure 10 using the layout standard throughout the paper. Considering the fact that the real integrator generates outputs proportional to the integrated acceleration only at frequencies higher than 0.1 Hz, the integrator has been included in the model used to predict the open loop sensor-actuator FRFs. For completeness the sensor-actuator open loop FRFs obtained assuming an ideal integrator have also been considered. As shown by the red lines in Figure 10, the real integrator causes a small additional semicircle in the locus depicted on the right hand side plot of Figure 10 (see the arrow in the zoomed area around the origin). This causes the locus to cross over the negative real axis at about 10 Hz. This effect is also visible in the Bode plots of Figure 10. In fact, the amplitudes of the sensor-actuator response roll-off rather steeply with frequency such that the additional cross-over occurring at 540 Hz is at an amplitude of at least 60 dB smaller than that at very low frequency produced by the response of the real integrator. The principal stability limit is therefore due to the real integrator frequency response function rather than the sensor-actuator coupling dynamics.

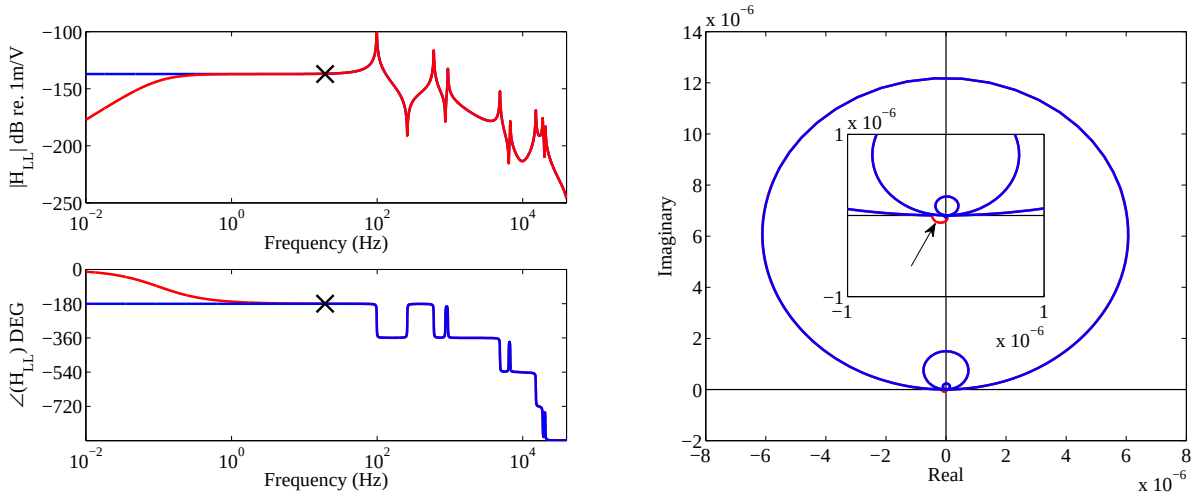


**Figure 10: Bode and Nyquist plots for the sensor-actuator open-loop frequency response functions: using an ideal double integrator (blue), and the real integrator having a 0.1 Hz cut-off frequency (red).**

The increase in the integrator cut-off frequency would cause the cross-over frequency also to increase. This would in turn also cause the increase in the open loop sensor-actuator FRF amplitude at the cross-over frequency, as it would approach the first resonance at 100 Hz. Thus the lower is the integrator cut-off frequency the higher is the stability margin. However, integration filters with very low cut-off frequency

require a large increase in the feedback gain and might also get more difficult to realise in practice due to the limitation on the electronics and especially due to the integrator drift. Nevertheless, as shown in the remaining of this study the 0.1 Hz integrators give plenty stability margin for large shifts in the absorber characteristic frequency. In order to determine this margin, the generalized Nyquist criterion was applied and the two eigenvalues of the return difference matrix obtained theoretically are shown in Figure 11 A and B, whereas the eigenvalues obtained experimentally are given in plots C and D.

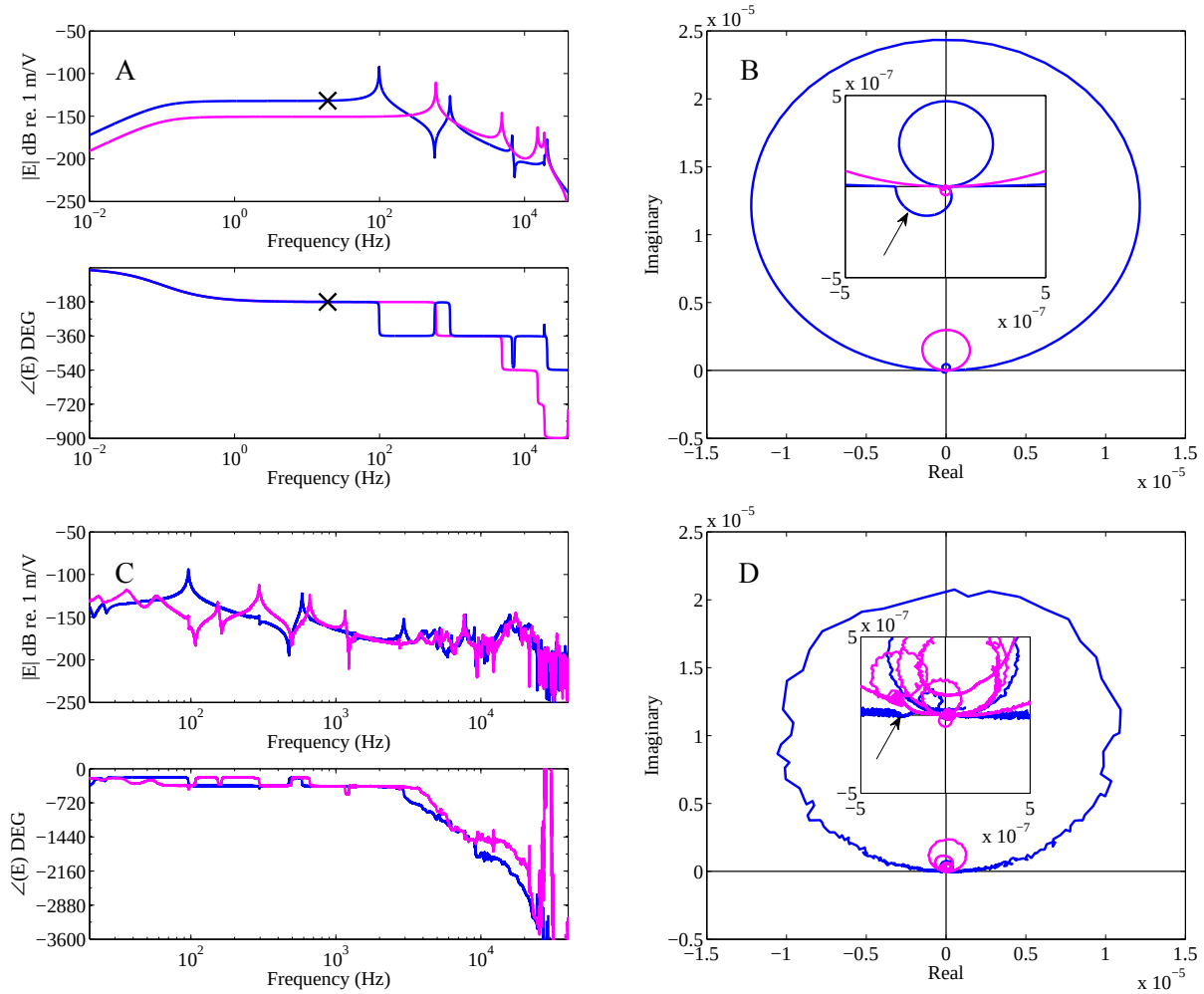


**Figure 11: Bode and Nyquist plots of the two eigenvalues of the return difference matrix QG obtained theoretically (plots A and B) and experimentally (plots C and D) with the double integrator having a cut-off frequency of 0.1 Hz.**

The Bode plots obtained from experimental measurements do not show the very low frequency region below 10 Hz as it was not measurable accurately due to a low coherence caused by the sensor signal-to-noise ratio, but in the Nyquist plot (D) it is possible to spot the cross over point at about 10 Hz in the zoomed area around the origin. The shapes of the Bode plots are rather similar, showing a favourable roll-off of the eigenvalue amplitudes with frequency and the Nyquist plots show that the largest circles have the $\Im$-axis as a symmetry line, which means that the two feedback loops are delivering active stiffness effects without the undesirable damping. The closed loop input accelerances are shown in Figure 12 where it can be seen that theoretically the maximum downward shift of the absorber characteristic frequency is almost -50 Hz as the resulting closed loop characteristic frequency is now 13 Hz. The lowest characteristic frequency achieved experimentally was 27 Hz, which is a considerable downshift of 35 Hz from the original 62 Hz. In conclusion, the active stiffness approach does not require heavy filtering for stability that causes the unwanted damping effects, and it still enables large adaptability of the tuneable vibration absorber studied.

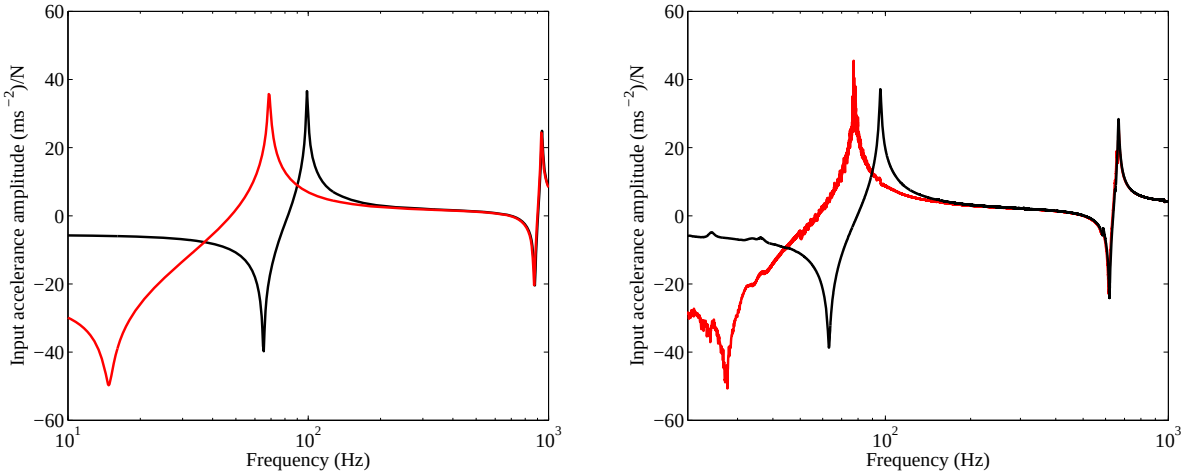


**Figure 12: Input accelerance at the absorber mounting point with open loops (black line), and closed loop using the maximum stable feedback gain.**

## Conclusions

The implementation of acceleration and displacement feedback control is applied on a beam-typed tuneable vibration absorber aiming to actively tune the absorber characteristic frequency. The two approaches are investigated and contrasted theoretically and experimentally using a mobility-impedance mathematical model and a prototype absorber. Although theoretically possible, the acceleration feedback approach fails in practice due to the intrinsic property of the open loop sensor-actuator frequency response functions (FRF), which exhibit amplitudes increasing with frequency. This causes stability problems as the sensor-actuator pair do not behave as collocated at higher frequencies. Furthermore, the control aims at shifting the rather low-frequency zero of the absorber input accelerance, whereas the open loop sensor-actuator FRF has only small amplitudes at low frequencies. As a result the implementation of the feedback loops with the available feedback gain yields almost no shift of the characteristic frequency. The low-pass filtering attempt resulted in a considerable improvement in the available feedback gain, however at cost of delivering an undesirable damping effect. In contrast, the implementation of displacement feedback is characterized by a sensor-actuator open loop FRF amplitude that rolls off rather steeply with frequency, such that the high frequency non-collocated behaviour of the sensor-actuator pairs is no longer relevant for the feedback loop stability. The principal stability limit is now set by the frequency response function of the double time-integrator rather than by the sensor-actuator coupling dynamics. With this second approach, the absorber characteristic frequency can be shifted down from 62 Hz by almost -50 Hz to 13 Hz. The lowest characteristic frequency accomplished experimentally was 27 Hz, which is a considerable downshift of 35 Hz from the original 62 Hz. The active stiffness approach seems to be a more feasible one, as it does not require heavy filtering for stability, and it still enables large adaptability of the tuneable vibration absorber characteristic frequency.

## Acknowledgements

The research performed by Neven Alujević was supported financially through a Research Training Network funded under the 6th Framework Programme of the European Commission “Smart Structures - A Computer Aided Engineering Approach to Smart Structures” (MRTN-CT-2006-035559), and through The National Foundation for Science, Higher Education and Technological Development of the Republic of Croatia, NZZ, post-doc program, project “ACTIVATE”.

## References


[1] J. Ormondroyd, J. P. den Hartog, *The Theory of the vibration absorber*. Transactions of the American Society of Mechanical Engineers 49, (1928), pp. A9-A22.

[2] J. B. Hunt**,** *Dynamic Vibration Absorbers***,** London: Mechanical Engineering Publications Ltd. (1979).

[3] D. J. Mead, *Passive Vibration Control*, New York: Wiley (1999)

[4] Den Hartog, J. P., *Mechanical Vibrations*, McGraw-Hill Book Co., New York, (1934.)

[5] J. van Dyke, J. Schendel, C. Gunderson and M. Ballard, *Cabin noise reduction in the DC-9*. AIAA paper 67-401, (1967)

[6] J. Q. Sun, M. R. Jolly and M. A. Norris, *Passive, adaptive and active tuned vibration absorbers - a survey*, Transactions of American Society of Mechanical Engineers Journal of Mechanical Design 117, (1995), pp. 234–242.

[7] A. H. von Flotow, A. Beard and D. Bailey *Adaptive tuned vibration absorbers: tuning laws, tracking agility, sizing and physical implementations.* Proceedings of Noise-Conference 94, (1994), pp. 437-454.

[8] M. J. Brennan *Vibration control using a tunable vibration neutralizer*. Proceedings of the Institution of Mechanical Engineers, Journal of Mechanical Engineering Science 211, (1997), pp. 91–108.

[9] P. L. Walsh and J. S. Lamancusa, *A variable stiffness vibration absorber for the minimisation of transient vibrations,* Journal of Sound and Vibration 158, (1992), pp. 195-211.

[10] M. J. Brennan *Actuators for active vibration control - tunable resonant devices,* Proceedings of the 4th European Conference on Smart Materials and Structures, Harrogate, UK, 6-8 July 1998, pp. 41-48.

[11] C. Q. Howard, *Review of adaptive tuned vibration neutralisers,* Proceedings of Acoustics 2009: Research to Consulting, the Annual Conference of the Australian Acoustical Society, University of Adelaide 23-23 November 2009. pp. 1-6.

[12] Ryan, M. W., Franchek, M. A., and Bernhard, R., *Adaptive-Passive Vibration Control of Single Frequency Excitations Applied to Noise Control*, 1994 Noise-Con Proceedings, pp. 461-466, Ft. Lauderdale, Florida, May 1994.

[13] M. A. Franchek, M.W. Ryan and R. J. Bernhard, *Adaptive passive vibration control*, Journal of Sound and Vibration 189, (1995), pp. 565-585.

[14] E. Rustighi, M.J. Brennan, and B.R. Mace, *A shape memory alloy adaptive tuned vibration absorber: Design and implementation*, Smart Materials and Structures, 14, 19-28, (2005)

[15] K. Williams, G. Chiu, R. Bernhard*, Adaptive-passive absorbers using shape-memory alloys*, Journal of Sound and Vibration 249 (5) (2002) 835–848.

[16] C. L. Davis and G. A. Lesieutre, *An Actively Tuned Solid-State Vibration Absorber Using Capacitive Shunting of Piezoelectric Stiffness*, Journal of Sound and Vibration, (2000), 232(3), pp. 601-617.

[17] R.A. Morgan, K.W. Wang, An active–passive piezoelectric absorber for structural vibration control under harmonic excitations with time-varying frequency, part 1: Algorithm development and analysis, Journal of Vibration and Acoustics-Transactions of the ASME 124 (1) (2002) 77–83.

[18] R.A. Morgan, K.W. Wang, An active–passive piezoelectric absorber for structural vibration control under harmonic excitations with time-varying frequency, part 2: Experimental validation and parametric study, Journal of Vibration and Acoustics-Transactions of the ASME 124 (1) (2002) 84–89.

[19] J. Tang, K.W. Wang, Active–passive hybrid piezoelectric networks for vibration control: comparisons and improvement, Smart Materials and Structures 10 (4) (2001) 794–806.

[20] N. Jalili, D.W. Knowles, Structural vibration control using an active resonator absorber: modelling and control implementation, Smart Materials and Structures 13 (5) (2004) 998–1005.

[21] N. Olgac, N. Jalili, *Modal analysis of flexible beams with delayed resonator vibration absorber: theory and experiments*, Journal of Sound and Vibration 218 (2) (1998) 307–331.

[22] Bartel, T.: *Entwicklung eines adaptiven Schwingungsabsorbers für ein Straßenbahnklimagerät*, Diplomarbeit, Technische Universität Darmstadt (2008).

[23] J. Bös, E. Janssen, M. Kauba, D. Mayer, *Reduction of compressor vibrations by means of an active tuned vibration absorber*, DAGA 2008, 34. Jahrestagung für Akustik, Dresden, (2008), pp. 315-316

[24] Sun J.Q., Some Observations on Physical Duality and Collocation of Structural Control Sensors and Actuators, Journal of Sound and Vibration, No. 194, pp. 765-770, 1996.

[25] Gardonio, P. and Brennan, M.J. *Advanced Applications in Acoustics, Noise and Vibration,* London, E & FN Spon, (2004), pp. 389-447

[26] S. J. Elliott, *Signal Processing for Active Control*, Academic Press, London, 2000.

## Appendix A

The elements of the matrix $\mathbf{Y}^{v,f}$ are the mobility functions relating velocities to forces between the locations defined in Equation (1):

$$\mathbf{Y}^{v,f} = \begin{bmatrix} Y^{v,f}_{m1,m1} & Y^{v,f}_{m1,m2} & Y^{v,f}_{m1,m3} & Y^{v,f}_{m1,c1} & Y^{v,f}_{m1,c2} & \cdots & Y^{v,f}_{m1,cM} & Y^{v,f}_{m1,e1} & Y^{v,f}_{m1,e2} & \cdots & Y^{v,f}_{m1,eN} \\ Y^{v,f}_{m2,m1} & Y^{v,f}_{m2,m2} & Y^{v,f}_{m2,m3} & Y^{v,f}_{m2,c1} & Y^{v,f}_{m2,c2} & \cdots & Y^{v,f}_{m2,cM} & Y^{v,f}_{m2,e1} & Y^{v,f}_{m2,e2} & \cdots & Y^{v,f}_{m2,eN} \\ Y^{v,f}_{m3,m1} & Y^{v,f}_{m3,m2} & Y^{v,f}_{m3,m3} & Y^{v,f}_{m3,c1} & Y^{v,f}_{m3,c2} & \cdots & Y^{v,f}_{m3,cM} & Y^{v,f}_{m3,e1} & Y^{v,f}_{m3,e2} & \cdots & Y^{v,f}_{m3,eN} \\ Y^{v,f}_{c1,m1} & Y^{v,f}_{c1,m2} & Y^{v,f}_{c1,m3} & Y^{v,f}_{c1,c1} & Y^{v,f}_{c1,c2} & \cdots & Y^{v,f}_{c1,cM} & Y^{v,f}_{c1,e1} & Y^{v,f}_{c1,e2} & \cdots & Y^{v,f}_{c1,eN} \\ Y^{v,f}_{c2,m1} & Y^{v,f}_{c2,m2} & Y^{v,f}_{c2,m3} & Y^{v,f}_{c2,c1} & Y^{v,f}_{c2,c2} & \cdots & Y^{v,f}_{c2,cM} & Y^{v,f}_{c2,e1} & Y^{v,f}_{c2,e2} & \cdots & Y^{v,f}_{c2,eN} \\ \vdots & \vdots & \vdots & \vdots & \vdots & \ddots & \vdots & \vdots & \vdots & \ddots & \vdots \\ Y^{v,f}_{cM,m1} & Y^{v,f}_{cM,m2} & Y^{v,f}_{cM,m3} & Y^{v,f}_{cM,c1} & Y^{v,f}_{cM,c2} & & Y^{v,f}_{cM,cM} & Y^{v,f}_{cM,e1} & Y^{v,f}_{cM,e2} & & Y^{v,f}_{cM,eN} \\ Y^{v,f}_{e1,m1} & Y^{v,f}_{e1,m2} & Y^{v,f}_{e1,m3} & Y^{v,f}_{e1,c1} & Y^{v,f}_{e1,c2} & & Y^{v,f}_{e1,cM} & Y^{v,f}_{e1,e1} & Y^{v,f}_{e1,e2} & & Y^{v,f}_{e1,eN} \\ Y^{v,f}_{e2,m1} & Y^{v,f}_{e2,m2} & Y^{v,f}_{e2,m3} & Y^{v,f}_{e2,c1} & Y^{v,f}_{e2,c2} & & Y^{v,f}_{e2,cM} & Y^{v,f}_{e2,e1} & Y^{v,f}_{e2,e2} & & Y^{v,f}_{e2,eN} \\ \vdots & \vdots & \vdots & \vdots & \vdots & \ddots & \vdots & \vdots & \vdots & \ddots & \vdots \\ Y^{v,f}_{eN,m1} & Y^{v,f}_{eN,m2} & Y^{v,f}_{eN,m3} & Y^{v,f}_{eN,c1} & Y^{v,f}_{eN,c2} & & Y^{v,f}_{eN,cM} & Y^{v,f}_{eN,e1} & Y^{v,f}_{eN,e2} & & Y^{v,f}_{eN,eN} \end{bmatrix}. \tag{A1}$$

The elements of the matrix $\mathbf{Y}^{\alpha,f}$ are the mobility functions relating the angular velocities to forces between all locations considered along the beam:

$$\mathbf{Y}^{\alpha,f} = \begin{bmatrix} Y^{\alpha,f}_{m1,m1} & Y^{\alpha,f}_{m1,m2} & Y^{\alpha,f}_{m1,m3} & Y^{\alpha,f}_{m1,c1} & Y^{\alpha,f}_{m1,c2} & \cdots & Y^{\alpha,f}_{m1,cM} & Y^{\alpha,f}_{m1,e1} & Y^{\alpha,f}_{m1,e2} & \cdots & Y^{\alpha,f}_{m1,eN} \\ Y^{\alpha,f}_{m2,m1} & Y^{\alpha,f}_{m2,m2} & Y^{\alpha,f}_{m2,m3} & Y^{\alpha,f}_{m2,c1} & Y^{\alpha,f}_{m2,c2} & \cdots & Y^{\alpha,f}_{m2,cM} & Y^{\alpha,f}_{m2,e1} & Y^{\alpha,f}_{m2,e2} & \cdots & Y^{\alpha,f}_{m2,eN} \\ Y^{\alpha,f}_{m3,m1} & Y^{\alpha,f}_{m3,m2} & Y^{\alpha,f}_{m3,m3} & Y^{\alpha,f}_{m3,c1} & Y^{\alpha,f}_{m3,c2} & \cdots & Y^{\alpha,f}_{m3,cM} & Y^{\alpha,f}_{m3,e1} & Y^{\alpha,f}_{m3,e2} & \cdots & Y^{\alpha,f}_{m3,eN} \\ Y^{\alpha,f}_{c1,m1} & Y^{\alpha,f}_{c1,m2} & Y^{\alpha,f}_{c1,m3} & Y^{\alpha,f}_{c1,c1} & Y^{\alpha,f}_{c1,c2} & \cdots & Y^{\alpha,f}_{c1,cM} & Y^{\alpha,f}_{c1,e1} & Y^{\alpha,f}_{c1,e2} & \cdots & Y^{\alpha,f}_{c1,eN} \\ Y^{\alpha,f}_{c2,m1} & Y^{\alpha,f}_{c2,m2} & Y^{\alpha,f}_{c2,m3} & Y^{\alpha,f}_{c2,c1} & Y^{\alpha,f}_{c2,c2} & \cdots & Y^{\alpha,f}_{c2,cM} & Y^{\alpha,f}_{c2,e1} & Y^{\alpha,f}_{c2,e2} & \cdots & Y^{\alpha,f}_{c2,eN} \\ \vdots & \vdots & \vdots & \vdots & \vdots & \ddots & \vdots & \vdots & \vdots & \ddots & \vdots \\ Y^{\alpha,f}_{cM,m1} & Y^{\alpha,f}_{cM,m2} & Y^{\alpha,f}_{cM,m3} & Y^{\alpha,f}_{cM,c1} & Y^{\alpha,f}_{cM,c2} & \cdots & Y^{\alpha,f}_{cM,cM} & Y^{\alpha,f}_{cM,e1} & Y^{\alpha,f}_{cM,e2} & \cdots & Y^{\alpha,f}_{cM,eN} \\ Y^{\alpha,f}_{e1,m1} & Y^{\alpha,f}_{e1,m2} & Y^{\alpha,f}_{e1,m3} & Y^{\alpha,f}_{e1,c1} & Y^{\alpha,f}_{e1,c2} & \cdots & Y^{\alpha,f}_{e1,cM} & Y^{\alpha,f}_{e1,e1} & Y^{\alpha,f}_{e1,e2} & \cdots & Y^{\alpha,f}_{e1,eN} \\ Y^{\alpha,f}_{e2,m1} & Y^{\alpha,f}_{e2,m2} & Y^{\alpha,f}_{e2,m3} & Y^{\alpha,f}_{e2,c1} & Y^{\alpha,f}_{e2,c2} & \cdots & Y^{\alpha,f}_{e2,cM} & Y^{\alpha,f}_{e2,e1} & Y^{\alpha,f}_{e2,e2} & \cdots & Y^{\alpha,f}_{e2,eN} \\ \vdots & \vdots & \vdots & \vdots & \vdots & \ddots & \vdots & \vdots & \vdots & \ddots & \vdots \\ Y^{\alpha,f}_{eN,m1} & Y^{\alpha,f}_{eN,m2} & Y^{\alpha,f}_{eN,m3} & Y^{\alpha,f}_{eN,c1} & Y^{\alpha,f}_{eN,c2} & \cdots & Y^{\alpha,f}_{eN,cM} & Y^{\alpha,f}_{eN,e1} & Y^{\alpha,f}_{eN,e2} & \cdots & Y^{\alpha,f}_{eN,eN} \end{bmatrix}. \tag{A2}$$

The elements of the matrix $\mathbf{Y}^{v,t}$ are the mobility functions relating the velocities to moments between all locations considered along the beam:

$$\mathbf{Y}^{v,t}=\begin{bmatrix} Y^{v,t}_{m1,m1} & Y^{v,t}_{m1,m2} & Y^{v,t}_{m1,m3} & Y^{v,t}_{m1,c1} & Y^{v,t}_{m1,c2} & \cdots & Y^{v,t}_{m1,cM} & Y^{v,t}_{m1,e1} & Y^{v,t}_{m1,e2} & \cdots & Y^{v,t}_{m1,eN} \\ Y^{v,t}_{m2,m1} & Y^{v,t}_{m2,m2} & Y^{v,t}_{m2,m3} & Y^{v,t}_{m2,c1} & Y^{v,t}_{m2,c2} & \cdots & Y^{v,t}_{m2,cM} & Y^{v,t}_{m2,e1} & Y^{v,t}_{m2,e2} & \cdots & Y^{v,t}_{m2,eN} \\ Y^{v,t}_{m3,m1} & Y^{v,t}_{m3,m2} & Y^{v,t}_{m3,m3} & Y^{v,t}_{m3,c1} & Y^{v,t}_{m3,c2} & \cdots & Y^{v,t}_{m3,cM} & Y^{v,t}_{m3,e1} & Y^{v,t}_{m3,e2} & \cdots & Y^{v,t}_{m3,eN} \\ Y^{v,t}_{c1,m1} & Y^{v,t}_{c1,m2} & Y^{v,t}_{c1,m3} & Y^{v,t}_{c1,c1} & Y^{v,t}_{c1,c2} & \cdots & Y^{v,t}_{c1,cM} & Y^{v,t}_{c1,e1} & Y^{v,t}_{c1,e2} & \cdots & Y^{v,t}_{c1,eN} \\ Y^{v,t}_{c2,m1} & Y^{v,t}_{c2,m2} & Y^{v,t}_{c2,m3} & Y^{v,t}_{c2,c1} & Y^{v,t}_{c2,c2} & \cdots & Y^{v,t}_{c2,cM} & Y^{v,t}_{c2,e1} & Y^{v,t}_{c2,e2} & \cdots & Y^{v,t}_{c2,eN} \\ \vdots & \vdots & \vdots & \vdots & \vdots & \ddots & \vdots & \vdots & \vdots & \ddots & \vdots \\ Y^{v,t}_{cM,m1} & Y^{v,t}_{cM,m2} & Y^{v,t}_{cM,m3} & Y^{v,t}_{cM,c1} & Y^{v,t}_{cM,c2} & \cdots & Y^{v,t}_{cM,cM} & Y^{v,t}_{cM,e1} & Y^{v,t}_{cM,e2} & \cdots & Y^{v,t}_{cM,eN} \\ Y^{v,t}_{e1,m1} & Y^{v,t}_{e1,m2} & Y^{v,t}_{e1,m3} & Y^{v,t}_{e1,c1} & Y^{v,t}_{e1,c2} & \cdots & Y^{v,t}_{e1,cM} & Y^{v,t}_{e1,e1} & Y^{v,t}_{e1,e2} & \cdots & Y^{v,t}_{e1,eN} \\ Y^{v,t}_{e2,m1} & Y^{v,t}_{e2,m2} & Y^{v,t}_{e2,m3} & Y^{v,t}_{e2,c1} & Y^{v,t}_{e2,c2} & \cdots & Y^{v,t}_{e2,cM} & Y^{v,t}_{e2,e1} & Y^{v,t}_{e2,e2} & \cdots & Y^{v,t}_{e2,eN} \\ \vdots & \vdots & \vdots & \vdots & \vdots & \ddots & \vdots & \vdots & \vdots & \ddots & \vdots \\ Y^{v,t}_{eN,m1} & Y^{v,t}_{eN,m2} & Y^{v,t}_{eN,m3} & Y^{v,t}_{eN,c1} & Y^{v,t}_{eN,c2} & \cdots & Y^{v,t}_{eN,cM} & Y^{v,t}_{eN,e1} & Y^{v,t}_{eN,e2} & \cdots & Y^{v,t}_{eN,eN} \end{bmatrix}. \tag{A3}$$

Finally, the elements of the matrix $\mathbf{Y}^{\alpha,t}$ are the mobility functions relating the angular velocities to moments between all locations considered along the beam:

$$\mathbf{Y}^{\alpha,t}=\begin{bmatrix} Y^{\alpha,t}_{m1,m1} & Y^{\alpha,t}_{m1,m2} & Y^{\alpha,t}_{m1,m3} & Y^{\alpha,t}_{m1,c1} & Y^{\alpha,t}_{m1,c2} & \cdots & Y^{\alpha,t}_{m1,cM} & Y^{\alpha,t}_{m1,e1} & Y^{\alpha,t}_{m1,e2} & \cdots & Y^{\alpha,t}_{m1,eN} \\ Y^{\alpha,t}_{m2,m1} & Y^{\alpha,t}_{m2,m2} & Y^{\alpha,t}_{m2,m3} & Y^{\alpha,t}_{m2,c1} & Y^{\alpha,t}_{m2,c2} & \cdots & Y^{\alpha,t}_{m2,cM} & Y^{\alpha,t}_{m2,e1} & Y^{\alpha,t}_{m2,e2} & \cdots & Y^{\alpha,t}_{m2,eN} \\ Y^{\alpha,t}_{m3,m1} & Y^{\alpha,t}_{m3,m2} & Y^{\alpha,t}_{m3,m3} & Y^{\alpha,t}_{m3,c1} & Y^{\alpha,t}_{m3,c2} & \cdots & Y^{\alpha,t}_{m3,cM} & Y^{\alpha,t}_{m3,e1} & Y^{\alpha,t}_{m3,e2} & \cdots & Y^{\alpha,t}_{m3,eN} \\ Y^{\alpha,t}_{c1,m1} & Y^{\alpha,t}_{c1,m2} & Y^{\alpha,t}_{c1,m3} & Y^{\alpha,t}_{c1,c1} & Y^{\alpha,t}_{c1,c2} & \cdots & Y^{\alpha,t}_{c1,cM} & Y^{\alpha,t}_{c1,e1} & Y^{\alpha,t}_{c1,e2} & \cdots & Y^{\alpha,t}_{c1,eN} \\ Y^{\alpha,t}_{c2,m1} & Y^{\alpha,t}_{c2,m2} & Y^{\alpha,t}_{c2,m3} & Y^{\alpha,t}_{c2,c1} & Y^{\alpha,t}_{c2,c2} & \cdots & Y^{\alpha,t}_{c2,cM} & Y^{\alpha,t}_{c2,e1} & Y^{\alpha,t}_{c2,e2} & \cdots & Y^{\alpha,t}_{c2,eN} \\ \vdots & \vdots & \vdots & \vdots & \vdots & \ddots & \vdots & \vdots & \vdots & \ddots & \vdots \\ Y^{\alpha,t}_{cM,m1} & Y^{\alpha,t}_{cM,m2} & Y^{\alpha,t}_{cM,m3} & Y^{\alpha,t}_{cM,c1} & Y^{\alpha,t}_{cM,c2} & \cdots & Y^{\alpha,t}_{cM,cM} & Y^{\alpha,t}_{cM,e1} & Y^{\alpha,t}_{cM,e2} & \cdots & Y^{\alpha,t}_{cM,eN} \\ Y^{\alpha,t}_{e1,m1} & Y^{\alpha,t}_{e1,m2} & Y^{\alpha,t}_{e1,m3} & Y^{\alpha,t}_{e1,c1} & Y^{\alpha,t}_{e1,c2} & \cdots & Y^{\alpha,t}_{e1,cM} & Y^{\alpha,t}_{e1,e1} & Y^{\alpha,t}_{e1,e2} & \cdots & Y^{\alpha,t}_{e1,eN} \\ Y^{\alpha,t}_{e2,m1} & Y^{\alpha,t}_{e2,m2} & Y^{\alpha,t}_{e2,m3} & Y^{\alpha,t}_{e2,c1} & Y^{\alpha,t}_{e2,c2} & \cdots & Y^{\alpha,t}_{e2,cM} & Y^{\alpha,t}_{e2,e1} & Y^{\alpha,t}_{e2,e2} & \cdots & Y^{\alpha,t}_{e2,eN} \\ \vdots & \vdots & \vdots & \vdots & \vdots & \ddots & \vdots & \vdots & \vdots & \ddots & \vdots \\ Y^{\alpha,t}_{eN,m1} & Y^{\alpha,t}_{eN,m2} & Y^{\alpha,t}_{eN,m3} & Y^{\alpha,t}_{eN,c1} & Y^{\alpha,t}_{eN,c2} & \cdots & Y^{\alpha,t}_{eN,cM} & Y^{\alpha,t}_{eN,e1} & Y^{\alpha,t}_{eN,e2} & \cdots & Y^{\alpha,t}_{eN,eN} \end{bmatrix}. \tag{A4}$$

The mobility functions $Y^{v,f}_{i,j}$, $Y^{\alpha,f}_{i,j}$, $Y^{v,t}_{i,j}$ and $Y^{\alpha,t}_{i,j}$ in Equation (A1-A4) between points defined by $x_i$ and $x_j$ have the following forms [25]:

$$Y^{v,F}_{i,j}(\omega)=j\omega\sum_{n=1}^{M}\frac{\phi_n(x_i)\phi_n(x_j)}{\rho bhl_x\left[\omega_n^2(1+j\eta)-\omega^2\right]}, \tag{A5a}$$

$$Y^{\alpha,F}_{i,j}(\omega)=j\omega\sum_{n=1}^{M}\frac{\frac{\partial\phi_n}{\partial x}(x_i)\phi_n(x_j)}{\rho bhl_x\left[\omega_n^2(1+j\eta)-\omega^2\right]}, \tag{A5b}$$

$$Y^{v,t}_{i,j}(\omega)=j\omega\sum_{n=1}^{M}\frac{\phi_n(x_i)\frac{\partial\phi_n}{\partial x}(x_j)}{\rho bhl_x\left[\omega_n^2(1+j\eta)-\omega^2\right]}, \tag{A5c}$$

$$Y^{\alpha,t}_{i,j}(\omega)=j\omega\sum_{n=1}^{M}\frac{\frac{\partial\phi_n(x_i)}{\partial x}\frac{\partial\phi_n(x_j)}{\partial x}}{\rho bhl_x\left[\omega_n^2(1+j\eta)-\omega^2\right]}, \tag{A5d}$$

where $j=\sqrt{-1}$, $\phi_n$ are the beam mode shapes, $\rho$ is the mass density of the beam material, $h$ is the beam thickness, $l_x$ is the beam length, $b$ is the beam width, $\omega_n$ are the beam natural frequencies, $\omega$ is the circular frequency, and $\eta$ is the loss factor. Details on how to calculate the natural frequencies and the mode shapes can be found in reference [25]. The modal summation in Equations (A5a-d) was truncated after including $M$=20 modes, and the twentieth mode has the corresponding resonance frequency of 281 kHz which is well above the upper bound of the usable sensor frequency range (0-17 kHz). The boundary conditions assumed for the calculation of mode shapes and natural frequencies are free-free.

## Appendix B

The matrix $\mathbf{Z}$ can be subdivided into four matrices as follows:

$$\mathbf{Z}=\begin{bmatrix}\mathbf{Z}^{f,v} & \mathbf{Z}^{t,v}\\ \mathbf{Z}^{f,\alpha} & \mathbf{Z}^{t,\alpha}\end{bmatrix}, \tag{B1}$$

where $\mathbf{Z}^{f,v}$ is the impedance matrix between the forces and velocities, $\mathbf{Z}^{t,v}$ is the impedance matrix between the moments and velocities, $\mathbf{Z}^{f,\alpha}$ is the impedance matrix between the forces and angular velocities, and finally $\mathbf{Z}^{t,\alpha}$ is the impedance matrix between beam bending moments and angular velocities. The matrix $\mathbf{Z}^{f,v}$ is diagonal and it is populated as follows:

$$\mathbf{Z}^{f,v}=\begin{bmatrix}
Z^{f,v}_{m1,m1} & 0 & 0 & 0 & 0 & 0 & 0 & 0 & 0 & 0 & 0\\
0 & Z^{f,v}_{m2,m2} & 0 & 0 & 0 & 0 & 0 & 0 & 0 & 0 & 0\\
0 & 0 & Z^{f,v}_{m3,m3} & 0 & 0 & 0 & 0 & 0 & 0 & 0 & 0\\
0 & 0 & 0 & Z^{f,v}_{c1,c1} & 0 & 0 & 0 & 0 & 0 & 0 & 0\\
0 & 0 & 0 & 0 & Z^{f,v}_{c2,c2} & 0 & 0 & 0 & 0 & 0 & 0\\
0 & 0 & 0 & 0 & 0 & \ddots & 0 & 0 & 0 & 0 & 0\\
0 & 0 & 0 & 0 & 0 & 0 & Z^{f,v}_{cM,cM} & 0 & 0 & 0 & 0\\
0 & 0 & 0 & 0 & 0 & 0 & 0 & Z^{f,v}_{e1,e1} & 0 & 0 & 0\\
0 & 0 & 0 & 0 & 0 & 0 & 0 & 0 & Z^{f,v}_{e2,e2} & 0 & 0\\
0 & 0 & 0 & 0 & 0 & 0 & 0 & 0 & 0 & \ddots & 0\\
0 & 0 & 0 & 0 & 0 & 0 & 0 & 0 & 0 & 0 & Z^{f,v}_{eN,eN}
\end{bmatrix}, \tag{B2}$$

where $Z^{f,v}_{m1,m1}=-j\omega m_1$, $Z^{f,v}_{m2,m2}=-j\omega m_2$, $Z^{f,v}_{m3,m3}=-j\omega m_3$. The impedances at the control locations are $Z^{f,v}_{c1,c1}\cdots Z^{f,v}_{cM,cM}=0$, since the mass loading of the piezoelectric actuators is neglected, and impedances at the element locations are $Z^{f,v}_{e1,e1}\cdots Z^{f,v}_{eM,eM}=0$ since there is no additional loading at the element locations. The matrix $\mathbf{Z}^{f,\alpha}$ is also diagonal and it is populated as follows:

$$\mathbf{Z}^{f,\alpha} = \begin{bmatrix} Z^{f,\alpha}_{m1,m1} & 0 & 0 & 0 & 0 & 0 & 0 & 0 & 0 & 0 & 0 \\ 0 & Z^{f,\alpha}_{m2,m2} & 0 & 0 & 0 & 0 & 0 & 0 & 0 & 0 & 0 \\ 0 & 0 & Z^{f,\alpha}_{m3,m3} & 0 & 0 & 0 & 0 & 0 & 0 & 0 & 0 \\ 0 & 0 & 0 & Z^{f,\alpha}_{c1,c1} & 0 & 0 & 0 & 0 & 0 & 0 & 0 \\ 0 & 0 & 0 & 0 & Z^{f,\alpha}_{c2,c2} & 0 & 0 & 0 & 0 & 0 & 0 \\ 0 & 0 & 0 & 0 & 0 & \ddots & 0 & 0 & 0 & 0 & 0 \\ 0 & 0 & 0 & 0 & 0 & 0 & Z^{f,\alpha}_{cM,cM} & 0 & 0 & 0 & 0 \\ 0 & 0 & 0 & 0 & 0 & 0 & 0 & Z^{f,\alpha}_{e1,e1} & 0 & 0 & 0 \\ 0 & 0 & 0 & 0 & 0 & 0 & 0 & 0 & Z^{f,\alpha}_{e2,e2} & 0 & 0 \\ 0 & 0 & 0 & 0 & 0 & 0 & 0 & 0 & 0 & \ddots & 0 \\ 0 & 0 & 0 & 0 & 0 & 0 & 0 & 0 & 0 & 0 & Z^{f,\alpha}_{eN,eN} \end{bmatrix}. \tag{B3}$$

The elements on the diagonal are $Z^{f,\alpha}_{m1,m1} = j\omega m_1 d$ , $Z^{f,\alpha}_{m2,m2} = 0$ , $Z^{f,\alpha}_{m3,m3} = -j\omega m_3 d$ , $Z^{f,\alpha}_{c1,c1} \ldots Z^{f,\alpha}_{cM,cM} = 0$ and $Z^{f,\alpha}_{e1,e1} \ldots Z^{f,\alpha}_{eN,eN} = 0$ , where the distance of the centre of gravity of the proof mass from the beam edge is designated as *d* (see Figure 2). The matrix $\mathbf{Z}^{t,v}$ has the same indexing layout as matrices $\mathbf{Z}^{f,v}$ and $\mathbf{Z}^{f,\alpha}$ . It is also diagonal and the elements on the diagonal are $Z^{t,v}_{m1,m1} = j\omega m_1 d$ , $Z^{t,v}_{m2,m2} = 0$ , $Z^{t,v}_{m3,m3} = -j\omega m_3 d$ , $Z^{t,v}_{c1,c1} \ldots Z^{t,v}_{cM,cM} = 0$ , $Z^{t,v}_{e1,e1} \ldots Z^{t,v}_{eN,eN} = 0$ . Finally the diagonal matrix $\mathbf{Z}^{t,\alpha}$ has the same indexing layout as matrices $\mathbf{Z}^{f,v}$ , $\mathbf{Z}^{f,\alpha}$ and $\mathbf{Z}^{t,v}$ with the elements on the diagonal $Z^{t,\alpha}_{m1,m1} = -I_{yy}$ , $Z^{t,\alpha}_{m2,m2} = 0$ , $Z^{t,\alpha}_{m3,m3} = -I_{yy}$ , $Z^{t,\alpha}_{c1,c1} \ldots Z^{t,\alpha}_{cM,cM} = 0$ , and $Z^{t,\alpha}_{e1,e1} \ldots Z^{t,\alpha}_{eN,eN} = 0$ .